iScience

CellPress
OPEN ACCESS

Article

MAPK pathway activation selectively inhibits ASCL1-driven small cell lung cancer

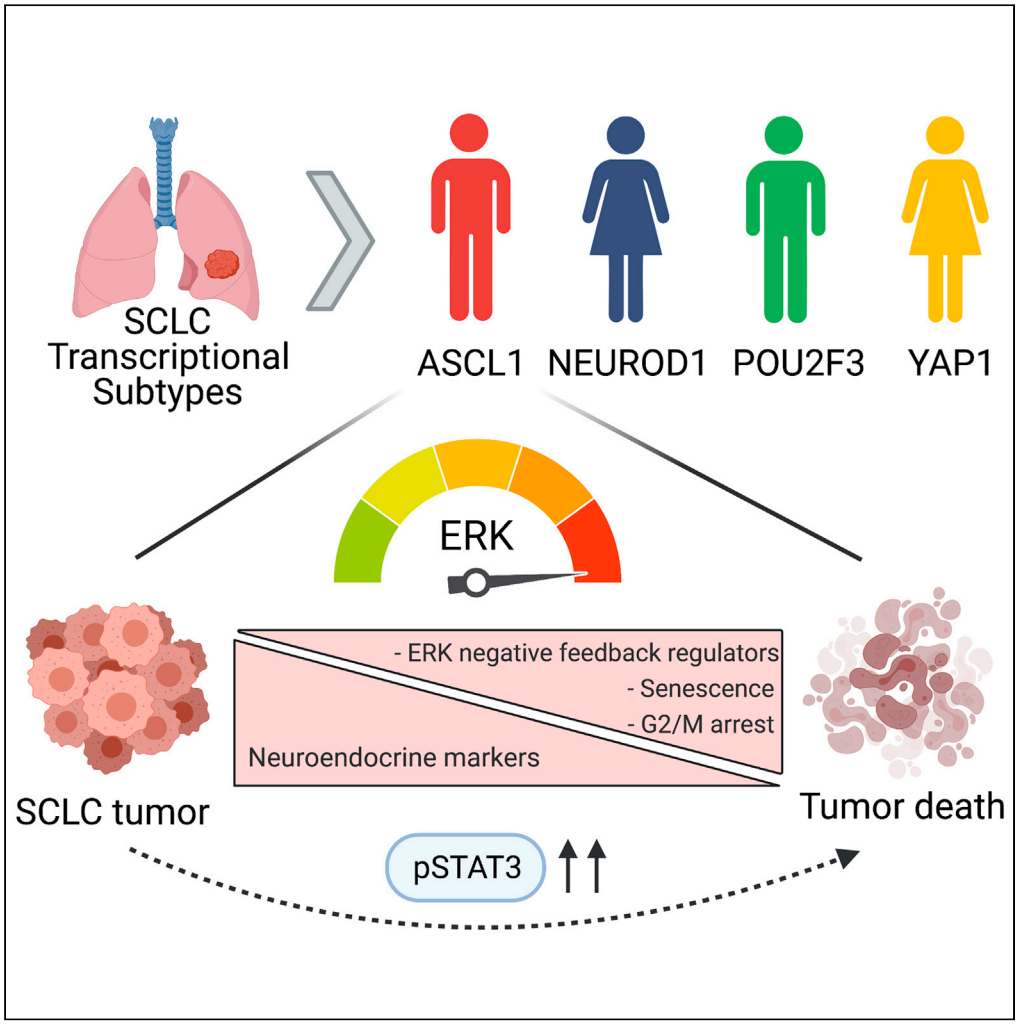

Rebecca Caeser, Christopher Hulton, Emily Costa, ..., John T. Poirier, Charles M. Rudin, Triparna Sen

rudinc@mskcc.org (C.M.R.)
sent@mskcc.org (T.S.)

Highlights

MAPK activation causes cell-cycle arrest and senescence selectively in SCLC-A subtype

MAPK-induced growth inhibition is independent of NOTCH signaling

MAPK activation increases ERK negative feedback and activates STAT3 signaling

Caeser et al., iScience 24, 103224
November 19, 2021
https://doi.org/10.1016/j.isci.2021.103224

iScience

CellPress
OPEN ACCESS

Article

MAPK pathway activation selectively inhibits ASCL1-driven small cell lung cancer

Rebecca Caeser,[1] Christopher Hulton,[2] Emily Costa,[1,3] Vidushi Durani,[1,3] Megan Little,[4] Xiaoping Chen,[5] Sam E. Tischfield,[6] Marina Asher,[7] Faruk Erdem Kombak,[7] Shweta S. Chavan,[1] Nisargbhai S. Shah,[1] Metamia Ciampricotti,[1,4] Elisa de Stanchina,[5] John T. Poirier,[8] Charles M. Rudin,[1,4,*] and Triparna Sen[1,4,9,*]

SUMMARY

Activation of mitogenic signaling pathways is a common oncogenic driver of many solid tumors including lung cancer. Although activating mutations in the mitogen-activated protein kinase (MAPK) pathway are prevalent in non-small cell lung cancers, MAPK pathway activity, counterintuitively, is relatively suppressed in the more aggressively proliferative small cell lung cancer (SCLC). Here, we elucidate the role of the MAPK pathway and how it interacts with other signaling pathways in SCLC. We find that the most common SCLC subtype, SCLC-A associated with high expression of *ASCL1*, is selectively sensitive to MAPK activation *in vitro* and *in vivo* through induction of cell-cycle arrest and senescence. We show strong upregulation of ERK negative feedback regulators and STAT signaling upon MAPK activation in SCLC-A lines. These findings provide insight into the complexity of signaling networks in SCLC and suggest subtype-specific mitogenic vulnerabilities.

INTRODUCTION

Small cell lung cancer (SCLC) is an aggressive malignancy, often demonstrating neuroendocrine features, that accounts for ~15% of all lung cancers in the United States (Bernhardt and Jalal, 2016; Hann et al., 2019). Metastasis is often found at first diagnosis, and metastatic disease is exceptionally lethal with a 2-year survival of <5% (Byers and Rudin, 2015). For decades, the primary treatment options for SCLC were limited to combination chemotherapy and radiotherapy; the emergence of resistant tumors commonly occurs within months for these treatment regimens. The therapeutic benefits of targeted therapies for SCLC have been generally disappointing, including inhibitors of PARP, CHK1, WEE1, and BCL2 (Poirier et al., 2020; Rudin et al., 2021). The addition of immune checkpoint blockade targeting the PD-1/PD-L1 axis has changed the first-line standard of care for metastatic SCLC but leads to durable response in only about 10% of patients (Horn et al., 2018; Paz-Ares et al., 2019; Rudin et al., 2020).

A major challenge to identifying effective treatments for SCLC is its association with the loss of key tumor suppressors, such as inactivating *RB1* and *TP53* alterations, but seems to lack targetable oncogenic driver mutations (George et al., 2015; Peifer et al., 2012; Rudin et al., 2012). Defining additional therapeutic options will depend on a deeper understanding of SCLC biology and the associated signaling pathways. Of note, SCLC has been recently subdivided into biologically distinct subtypes based on differential expression of key transcriptional regulators (*ASCL1*, *NEUROD1*, *POU2F3*, *YAP1*), defining subtypes SCLC-A, -N, -P, and -Y, respectively (Rudin et al., 2019). The role of YAP1 as a subtype-defining factor has subsequently been called into question (Baine et al., 2020; Pearsall et al., 2020). Emerging data suggest that these subtypes may respond differently to therapy (Gay et al., 2021; Owonikoko et al., 2021; Poirier et al., 2020).

The mitogen-activated protein kinase (MAPK) pathway is a central axis driving aberrant proliferation in a broad spectrum of cancers. Although somatic gain-of-function mutations in MAPK genes occur in about 30% of human cancers (Schubbert et al., 2007), including non-small cell lung cancer (NSCLC), genomic and proteomic analyses indicate suppression of MAPK pathway activity in SCLC (Byers et al., 2012; Cerami et al., 2012; Gao et al., 2013; Wagle et al., 2018). This striking difference is not well understood, and previous attempts to determine whether deficits in MAPK signaling might be therapeutically important in SCLC

[1]Department of Medicine, Memorial Sloan Kettering Cancer Center, New York, NY 10065, USA

[2]Louis V. Gerstner Jr. Graduate School of Biomedical Sciences, Memorial Sloan Kettering Cancer Center, New York, NY 10065, USA

[3]Weill Cornell Graduate School of Medical Sciences, Weill Cornell Medicine, New York, NY, USA

[4]Molecular Pharmacology Program, Memorial Sloan Kettering Cancer Center, New York, NY 10065, USA

[5]Antitumor Assessment Core Facility, Memorial Sloan Kettering Cancer Center, New York, NY 11065, USA

[6]Marie-Josée and Henry R. Kravis Center for Molecular Oncology, Memorial Sloan Kettering Cancer Center, New York, NY, USA

[7]Precision Pathology Center, Memorial Sloan Kettering Cancer Center, New York, NY 10065, USA

[8]Perlmutter Cancer Center, New York University Langone Health, New York, NY, USA

[9]Lead contact

*Correspondence: rudinc@mskcc.org (C.M.R.), sent@mskcc.org (T.S.)

https://doi.org/10.1016/j.isci.2021.103224

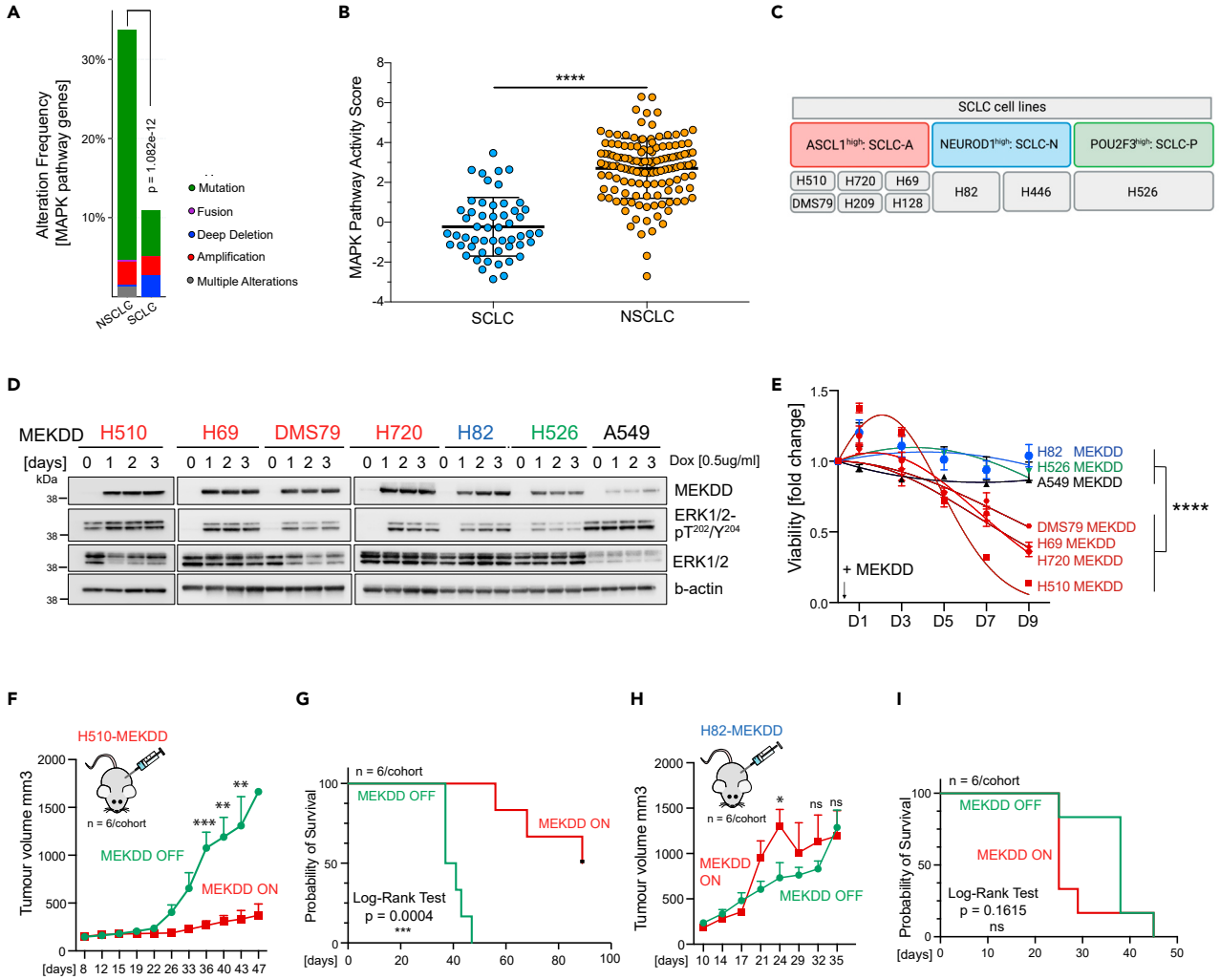

Figure 1. SCLC-A is selectively sensitive to MAPK activation *in vitro* and *in vivo*

(A) Bar graph showing absolute counts for Mutation, Fusion, Deep Deletion, Amplification, and Multiple Alterations found in MAPK pathway genes (KRAS, HRAS, BRAF, RAF1, MAP3K1, MAP2K1, MAP2K2, MAP2K4, MAPK1, DUSP4, and CCND1) comparing SCLC (n = 469) and NSCLC (n = 8,948) clinical samples. The dataset was derived from the MSK-IMPACT clinical sequencing cohort (Cerami et al., 2012; Gao et al., 2013) as of 24 March, 2021, with variants of unknown significance and germline mutation excluded. p Value derived from Pearson's *chi*-squared test considering all alterations.

(B) Graph showing MAPK Pathway Activity Score (*SPRY2*, *SPRY4*, *ETV4*, *ETV5*, *DUSP4*, *DUSP6*, *CCND1*, *EPHA2*, and *EPHA4)* comparing SCLC (n = 53) and NSCLC (n = 133) cell lines (±SD). MPAS was calculated as in Wagle et al. (2018) using *Z* scores for each gene/cell line from CCLE. Unpaired t test was performed between SCLC and NSCLC so that ****p < 0.0001.

(C) Overview of SCLC cell lines and their subtype used in this study. ASCL1-driven (SCLC-A, red), NEUROD1-driven (SCLC-N, blue), and POU2F3-driven (SCLC-P, green).

(D) Western blot analysis on ASCL1-driven (H510, H69, DMS79, H720, red), NEUROD1-driven (H82, blue), POU2F3-driven (H526, green) SCLC cell lines and NSCLC cell line A549 upon $MEKDD^{S217D/S221D}$ expression (0, 1, 2, 3 days). $MEKDD^{S217D/S221D}$ (HA-tag) and total and phosphorylated ERK1/2 are shown, and β-actin was used as loading control.

(E) Cell viability assay with SCLC cell lines following $MEKDD^{S217D/S221D}$ expression for 9 days. Illustrated are the average relative changes (±SEM) of cell viability. Unpaired t test was performed between *ASCL1*-driven (DMS79, H69, H720, H510) and non-*ASCL1*-driven (H82, H526, A549) SCLC cells so that ****p < 0.0001.

(F) ASCL1-driven SCLC cell line H510-MEKDD was injected subcutaneously into athymic mice (n = 6/cohort) and checked biweekly for palpable tumors. Mice in the "MEKDD ON" cohort were kept on a doxycycline chow diet throughout the experiment. Graph illustrates average tumor volume (mm^3, ±SEM) over time. Unpaired t test was performed between the two cohorts at the indicated time point so that **p < 0.01, ***p < 0.001.

(G) Overall survival of the recipient mice from **F** is plotted as a Kaplan-Meier curve and denoted as the time from injection of cells to tumor volume of 1,500 mm^3. p Value was calculated by log rank test.

Figure 1. *Continued*

(H) NEUROD1-driven SCLC cell line H82-MEKDD was injected subcutaneously into athymic mice (n = 6/cohort) and checked biweekly for palpable tumors. Mice in the "MEKDD ON" cohort were kept on a doxycycline chow diet throughout the experiment. Graph illustrates tumor volume (mm^3, ±SEM) over time. Unpaired t test was performed between the two cohorts at the indicated time point so that *$p < 0.05$, ns > 0.05. (I) Overall survival of the recipient mice from H is plotted as a Kaplan-Meier curve and denoted as the time from injection of cells to tumor volume of 1,500 mm^3. p Value was calculated by log rank test.

(Cristea et al., 2020; Cristea and Sage, 2016; Park et al., 2003; Ravi et al., 1998, 1999) have been discordant. One potential explanation for this disparity is that the recently described SCLC subtypes, differing in transcriptional signatures and therapeutic vulnerabilities, may also differ in their mitogenic signaling dependencies.

Here, we sought to elucidate the distinctions between and potential therapeutic vulnerabilities of MAPK pathway activation in different subtypes of SCLC. We show that activation of the MAPK pathway is particularly disadvantageous to the predominant SCLC-A subtype, associated with high expression of *ASCL1*. We link this sensitivity to downstream effects on other signaling pathways such as the STAT3 pathway. This study sheds light on the complexity and diversity of oncogenic signaling networks in SCLC, supporting that SCLC subtypes have distinct mitogenic signaling that may result in differential therapeutic vulnerabilities.

RESULTS

SCLC-A is selectively sensitive to MAPK activation

In contrast to NSCLC, genomic and proteomic analyses have indicated suppression of MAPK pathway activity in SCLC. We first assessed the frequency of somatic mutations in MAPK pathway mutations in our patients with lung cancer, profiled by MSK-IMPACT targeted tumor sequencing (Cheng et al., 2015). In a total of 8,948 patients with NSCLC and 469 patients with SCLC, MAPK pathway mutations in *KRAS*, *HRAS*, *BRAF*, *RAF1*, *MAP3K1*, *MAP2K1*, *MAP2K2*, *MAP2K4*, *MAPK1*, *DUSP4*, and *CCND1* were found in 3,021 (34%) of the NSCLC cohort in comparison with 51 (11%) of the SCLC cohort (Figures 1A and S1A) (Cerami et al., 2012; Gao et al., 2013). A breakdown of mutation frequency of individual genes revealed KRAS to be the most prominent mutation in the NSCLC and SCLC cohorts (29.1% and 3.2%, respectively) followed by BRAF in the NSCLC cohort (4.1%) and MAP2K4 in the SCLC cohort (2.5%) (Figure S1B). SCLC also has a significantly lower transcriptional MAPK Pathway Activity Score (MPAS; *SPRY2*, *SPRY4*, *ETV4*, *ETV5*, *DUSP4*, *DUSP6*, *CCND1*, *EPHA2*, *and EPHA4*) in comparison with NSCLC (Figure 1B). This finding is in keeping with prior protein-based analyses of 34 SCLC and 74 NSCLC cell lines by reverse-phase protein array, suggesting less activation of the MAPK pathway in SCLC relative to NSCLC (Byers et al., 2012). These striking differences in MAPK activity and targeting between SCLC and NSCLC are not well understood. We hypothesized that the molecular differences in recently recognized SCLC subtypes might explain the inconsistent results from prior studies examining the apparent MAPK pathway suppression in SCLC.

To initially assess this hypothesis, we examined the phenotypic differences that result from exogenous MAPK activation in a cohort of SCLC cell lines and an NSCLC control. We transduced cell lines from the three predominant SCLC subtypes (SCLC-A ($ASCL1^{high}$): H510, H720, H69, DMS79, H209, and H128; SCLC-P ($POU2F3^{high}$): H526; SCLC-N ($NEUROD1^{high}$): H82 and H446) and the NSCLC cell line A549 with a doxycycline-inducible vector driving expression of $MEKDD^{S217D/S221D}$ (MEK1) (Figure 1C). Table S1 shows cell lines used in this study with annotation of MAPK pathway alterations. Activation of the MAPK pathway through $MEKDD^{S217D/S221D}$ was confirmed, resulting in an increase in ERK phosphorylation as early as 24 h after activation (Figure 1D). The NSCLC cell line A549 harbors a $KRAS^{G12S}$ mutation and therefore has high baseline ERK phosphorylation levels, which are not further increased by $MEKDD^{S217D/S221D}$ expression. We next assessed how the different SCLC subtypes and NSCLC cell line respond over time to dox-induced expression of $MEKDD^{S217D/S221D}$. Expression of $MEKDD^{S217D/S221D}$ in NSCLC, SCLC-N, and SCLC-P subtype lines consistently showed no negative impact on viability (Figure 1E). However, ASCL1-driven SCLC cell lines (SCLC-A) were markedly sensitive to MAPK activation (Figures 1E and S1C), resulting in a mean decrease in cell viability of 67% at day 9.

We further tested the effects of exogenous MAPK activation on tumor growth in two SCLC-A lines and one SCLC-N line established as *in vivo* xenografts. H510 cells transduced with $MEKDD^{S217D/S221D}$ were injected into athymic mice (n = 6/cohort), which resulted in a significantly smaller tumor volume and longer survival in the cohort of mice receiving a doxycycline chow diet (MEKDD activated) relative to no-doxycycline controls (Figures 1F and 1G). H510 tumors in which MEKDD was activated demonstrated tumor growth inhibition of over 75% at 36 days relative to tumors without MAPK pathway activation (267 versus 1,076 mm^3

tumor volume, respectively). No significant difference between mean body weights was seen (Figure S1D). Similar results were observed in another SCLC-A cell line H720 (Figures S1E–S1G). Regardless of whether MEKDD expression was induced in H720 or not, histological examination revealed retention of SCLC characteristics, including solid sheets and clusters of round/oval blue cells with scant cytoplasm, nuclei with fine chromatin, high mitotic rate, no distinct nucleoli, occasional molding, and smudging (Figure S1H). H510 cells exhibited classical SCLC morphology with solid, nested, and trabecular architecture. H510 tumor cells without MEKDD expression exhibited somewhat more loosely packed nests and trabeculae with occasional solid foci, whereas upon MEKDD expression, tumor cells revealed predominantly solid sheets of tumor cells. Tumor cells from both models (H510 and H720) stained positive for the subtype marker ASCL1 and neuroendocrine markers INSM1 and NCAM1, regardless of MEKDD expression (Figure S1H). H82 (SCLC-N) cells that were transduced with MEKDD$^{S217D/S221D}$ and injected into athymic mice demonstrated the opposite phenotype. H82 tumors in which MEKDD was activated resulted in faster tumor formation relative to no-doxycycline controls (1,305 versus 734 mm^3, respectively) at day 24 and shorter survival (Figures 1H and 1I). No significant difference between mean body weights was seen (Figure S1I). Taken together these findings demonstrate a subtype-specific suppression of cell viability and tumor growth arrest of SCLC-A in *in vitro* and *in vivo* models, respectively, upon MAPK signaling activation.

MAPK activation in SCLC-A leads to a G2/M cell-cycle arrest and senescence

We next sought to further interrogate the cell growth and proliferative implications of aberrant MAPK activation in SCLC-A. Previous reports indicate that activation of the MAPK pathway via NRAS^{G12D}/RAS^{V12} alterations or an activatable form of c-raf-1 can lead to morphological changes in several different cancer types (Calbo et al., 2011; Ravi et al., 1998, 1999; Shieh et al., 2013; Yu and Garcia, 2020). Indeed, we observed that ERK activation in SCLC-A cell lines led cells that typically grow in suspension to adapt a more adherent phenotype. This was primarily seen in H69 and DMS79 SCLC-A cell lines (Figure 2A). Of interest, H510 cells that grow in culture as intermixed adherent and suspension populations fully change to suspension cells, increasing the number of floating clusters of cells as early as 24 h after MAPK activation and becoming a fully apparent shift by day 3 (Figure 2A). No change in morphology was observed in SCLC-A H720 and SCLC-N and -P lines H82 and H526, respectively.

SCLC-A cell lines are notable for high-level expression of both ASCL1 and INSM1, two transcription factors implicated in driving neuroendocrine cell fate (Borges et al., 1997; Borromeo et al., 2016). Lim et al. observed that upon NOTCH activation, neuroendocrine cells adopt a non-neuroendocrine phenotype (Lim et al., 2017). Given that prior reports had correlated ERK activation with NOTCH induction (Tremblay et al., 2013), we proceeded to check ASCL1 and INSM1 expression levels upon MAPK pathway activation. We observed a decrease in ASCL1 and INSM1 protein levels 24 h after MAPK activation in all SCLC-A cell lines, although to variable extents, with the most marked suppression of both in H510 (Figure 2B). SCLC-N, SCLC-P, and NSCLC cells had no detectable ASCL1 expression. A modest decrease in INSM1 was observed in H526 (SCLC-P) after 48 h; levels of NEUROD1 and POU2F3 were unaffected (Figure 2B).

As the most notable morphological change was observed in H69 cells, we proceeded to culture these cells long term, separating the adherent and suspension cells. MAPK activation resulted in similar decreases in ASCL1 and INSM1 expression in adherent and suspension H69 cells cultured separately over 4 weeks (Figure 2C). However, gene expression for the neuroendocrine factor synaptophysin (SYP) seemed to be selectively depleted in the adherent cell population. The morphological change and decrease in neuroendocrine marker expression are suggestive of an epithelial-to-mesenchymal transition (EMT) phenotype, which prompted us to analyze well-known EMT markers. Indeed, adherent cells exclusively induced expression of E-cadherin, N-cadherin, Vimentin, and NOTCH1; none of these factors were appreciably altered in suspension cells (Figure 2C).

We next investigated the mechanism of growth arrest in SCLC-A models upon MAPK activation. We explored two alternative possibilities leading to cell growth abrogation—apoptosis or cell-cycle arrest. There were no significant increases in apoptosis, as measured by annexin V staining, even after 5 days of MAPK activation in SCLC-A cells (Figure 2D). In addition, growth inhibition upon MAPK activation could not be reversed through treatment with z-VAD-FMK (20 μM, day 6), an irreversible pan-caspase inhibitor that blocks apoptosis (Figure S2A).

Cell cycle profiling revealed that MAPK activation in H510 cells resulted in a significant accumulation of cells in the G2/M phase ($p < 0.0001$) accompanied by a significant S phase depletion ($p = 0.0014$) by 2 days

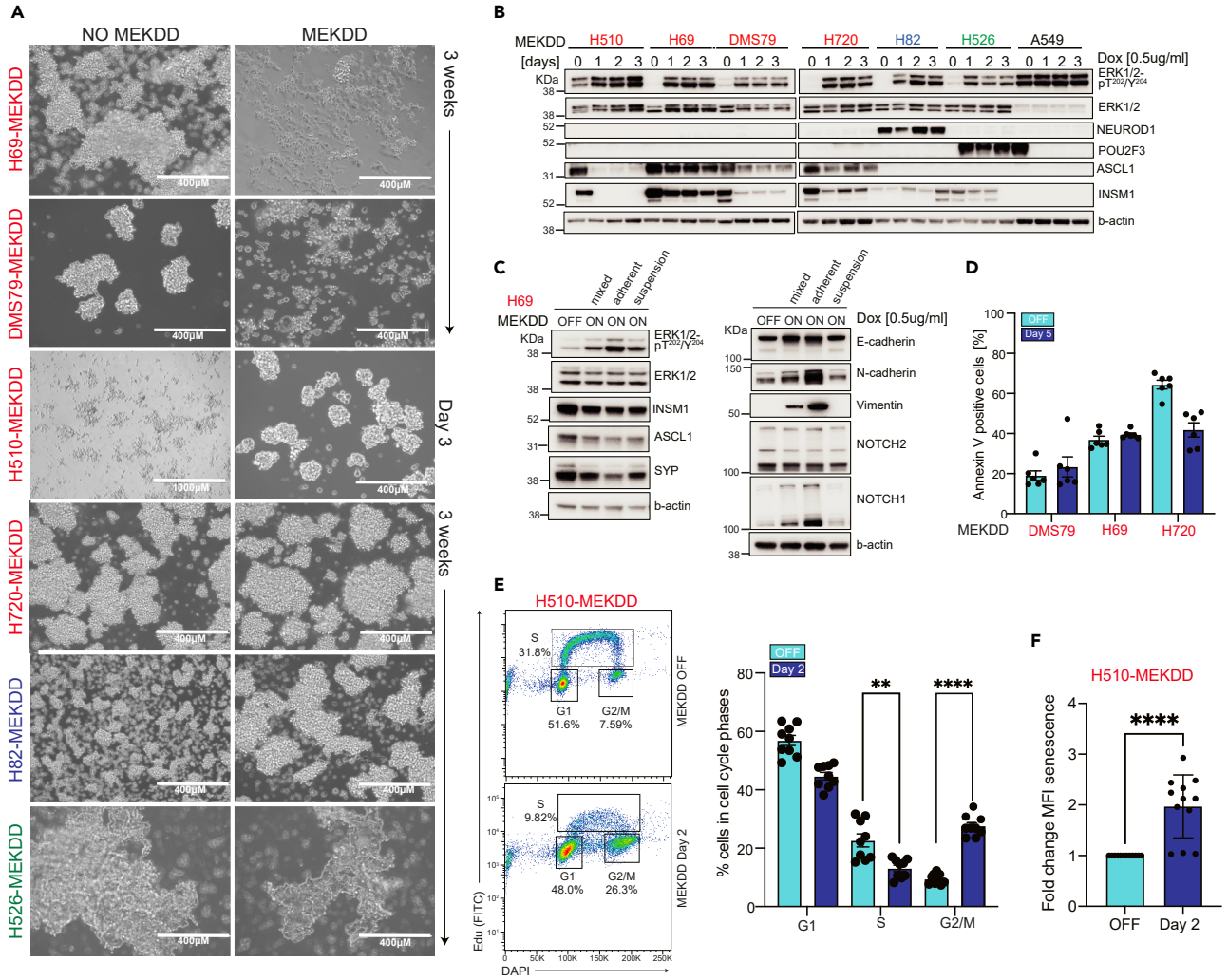

Figure 2. MAPK activation in SCLC-A leads to a G2/M cell-cycle arrest and senescence

(A) Images were taken of SCLC cell lines with and without MEKDD$^{S217D/S221D}$ expression at the indicated time points. Scale bar as indicated in every image (400 or 1,000 μM).

(B) Western blot analysis on SCLC cell lines as indicated upon MEKDD$^{S217D/S221D}$ expression (0, 1, 2, 3 days). Total and phosphorylated ERK1/2, NEUROD1, POU2F3, ASCL1, and INSM1 are shown with β-actin used as loading control.

(C) Western blot analysis on ASCL1-driven SCLC cell line H69 cultured as adherent, suspension, and mixed upon MEKDD$^{S217D/S221D}$ expression at day 28. Total and phosphorylated ERK1/2, INSM1, ASCL1, and SYP are shown with β-actin used as loading control (left). E- and N-Cadherin, Vimentin, NOTCH1, and NOTCH2 are shown with β-actin used as loading control (right).

(D) Cell survival following MEKDD$^{S217D/S221D}$ expression in DMS79, H69, and H720 was monitored by annexin-V and DAPI staining and analyzed by flow cytometry at day 5. Bar chart illustrates annexin V-positive cells for the indicated cell line (n = 6, ±SEM).

(E) Cell cycle analysis following MEKDD$^{S217D/S221D}$ expression in H510 was monitored by Click-iT Edu and DAPI and analyzed by flow cytometry at day 2. Bar chart illustrates percentage of cells in the indicated cycle phase (n = 9, ±SEM). Unpaired t test was performed so that **$p < 0.01$, ****$p < 0.0001$. (F) Senescence analysis following MEKDD$^{S217D/S221D}$ expression in H510 was monitored by CellEvent Senescence and analyzed by flow cytometry at day 2. Bar chart illustrates fold change of mean fluorescence intensity (n = 12, ±SEM). Unpaired t test was performed so that ****$p < 0.0001$.

(Figure 2E). We also observed a 2-fold increase ($p < 0.0001$) in senescent cells, as indicated by β-galactosidase hydrolysis, upon MAPK activation in H510 (Figure 2F). As mentioned earlier, H510 without MAPK activation grows as intermixed adherent and suspension cells, and for the analysis of β-galactosidase hydrolysis via flow cytometry, the adherent and suspension cell populations were not separated but measurement was taken from the mixed population. Upon MAPK activation, the intermixed populations fully change to suspension cells and were used for flow cytometric quantification. A similar observation (mean 3-fold increase in senescent cells, $p = 0.0002$) was seen in H720 after 7 days (Figure S2B). The increase

in senescent cells was accompanied by an increase in p27 protein expression in H510 and H720 cells (Figure S2C). Together these data suggest that MAPK activation does not cause apoptosis but instead induces G2 cell-cycle arrest and senescence in SCLC-A cells.

ERK-induced growth inhibition is independent of NOTCH and its target genes, HES1 and JAG1

To identify the transcriptomic changes induced by MAPK activation, we next performed bulk RNA sequencing of SCLC cell lines (n = 6) across three subtypes after 24 h of MEKDD$^{S217D/S221D}$ expression. As previously seen at the protein level, we observed that *INSM1* expression in SCLC-A cells (H69, H720, H209) was significantly decreased by MAPK activation relative to changes seen in non-SCLC-A cells (H82, H446, H526; p = 0.0137, Figure S2D). No significant difference in *ASCL1* expression was observed.

We observed an enrichment of gene expression in NOTCH family genes including *JAG1*, *HES1*, *and REST* (Figure 3A, p = 0.14, 0.05, and 0.0027, respectively) in SCLC-A cells compared with non-SCLC-A cells. This is in agreement with previous reports of NOTCH activation in SCLC, including an increase in HES1 expression associated with cell-cycle arrest (Lim et al., 2017; Sriuranpong et al., 2001; Tremblay et al., 2013). We next investigated whether deletion of NOTCH target genes would rescue growth inhibition upon MAPK activation in our model. We disrupted the *HES1* and *JAG1* genes via CRISPR-Cas9 using two gRNAs against HES1 and three gRNAs against JAG1. Knockout of *HES1* did not rescue cell growth inhibition (Figure 3B) or protein re-expression of ASCL1 and INSM1 (Figure 3C). All gRNAs led to effective depletion of HES1 (Figure 3C). Similar results were observed with JAG1 knockdown (Figures 3D and 3E). Effective depletion of JAG1 was confirmed on protein level, and with NOTCH1 being downstream of JAG1, a decrease in cleaved NOTCH1 expression was also seen upon JAG1 knockdown (Figure 3E).

Genetic disruption of NOTCH signaling did not rescue ERK-mediated growth inhibition or loss of lineage oncogenes, suggesting NOTCH signaling does not regulate ASCL1 or growth downstream of ERK. This is in agreement with prior data showing that NOTCH activity as a tumor suppressor or protooncogene is highly context dependent (Lim et al., 2017).

MAPK activation increases ERK negative feedback and activates STAT3

The observation that SCLC-A cells are sensitive to MAPK signaling activation prompted us to examine the key molecular changes in these models. Previous work established that hyperactivation of BRAF^{V600E}, RAS, and MYC can result in oncogene-induced senescence (Michaloglou et al., 2005; Serrano et al., 1997) in some solid tumors and pre-B acute lymphoblastic leukemia, associated with upregulation of negative feedback on MAPK signaling through factors such as SPRY2, DUSP6, and ETV5 (Courtois-Cox et al., 2006; Shojaee et al., 2015). Thus, we next investigated whether upregulation of ERK negative regulators could be observed in SCLC models (Figure 4A). MAPK activation significantly upregulated the expression of DUSP6 and SPRY2, but not ETV5 proteins, in a time-dependent manner (24–72 h) in SCLC-A cell lines (Figure 4B); the response was blunted or absent in SCLC-N (H82), SCLC-P (H526), or NSCLC (A549) cells. Bulk RNA sequencing 24 h after MAPK activation was assessed for differential gene expression of DUSP and SPRY family members (Figure 4C); of these, DUSP6 was consistently differentially induced in the SCLC-A versus non-SCLC-A lines (1.7-fold increase; p = 0.0049). Of interest, MAPK activation appeared to selectively increase DUSP6 and SPRY2 protein expression in adherent H69 cells but not in H69 cells in suspension (Figure 4D). This suggests that the transition from neuroendocrine to non-neuroendocrine phenotype in this setting might be associated with ERK negative feedback.

To more broadly interrogate the signaling network induced by MAPK activation, we performed a phosphokinase array in SCLC-A (H720 and H69) and SCLC-N (H82) cells. Surprisingly, signaling changes in protein kinase phosphorylation upon MAPK activation were limited. The most striking change, apart from the expected increase in ERK phosphorylation, was a significant increase in STAT3 phosphorylation on serine 727 (Figures 4E and S3A). This was only seen in SCLC-A cell lines (p = 0.0001) (Figure 4F). The increase in STAT3-pS^{727} was verified in additional SCLC-A cell lines (H510, DMS79) and was not observed in SCLC-N (H82), SCLC-P (H526), and NSCLC (A549) cells (Figure 4G). The observed increases in ERK negative feedback regulators DUSP6 and SPRY2, as well as the increase in STAT3-pS^{727}, were also maintained at the protein level in tumors from *in vivo* models injected with H720 MEKDD cells (described in Figures S1E and S1F) with variability seen between mice (Figure S3B).

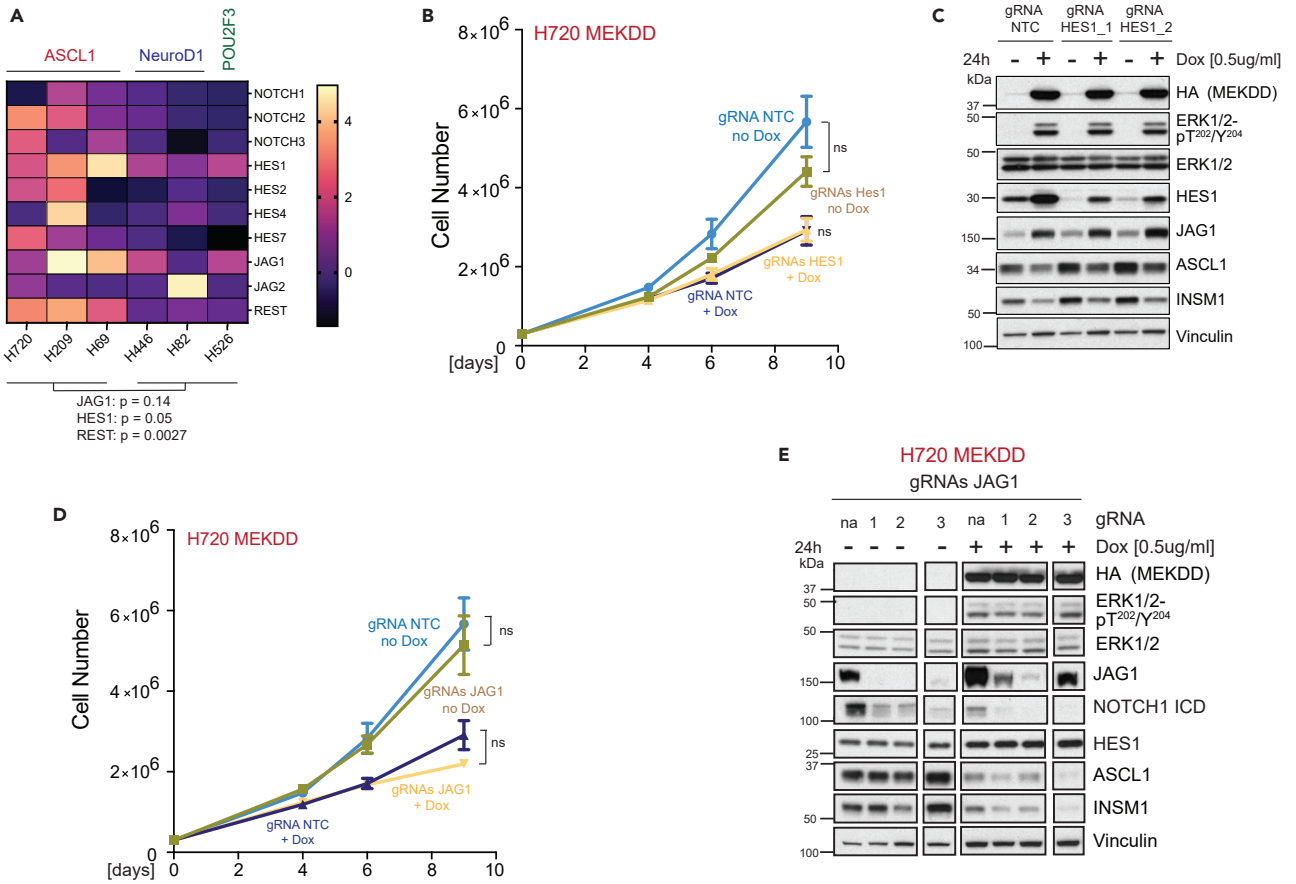

Figure 3. ERK-induced growth inhibition is independent of NOTCH and its target genes, HES1 and JAG1

(A) Heatmap of SCLC cell lines showing log2 fold change for relative change in gene expression after MEKDD$^{S217D/S221D}$ expression (24 h). Unpaired t test was performed between *ASCL1*- and non-*ASCL1*-SCLC cell lines with p value as indicated.

(B) H720/MEKDD was transduced with Cas9 and gRNAs against HES1 (n = 2, ±SEM) and NTC (n = 1, ±SEM). Following transduction with gRNAs, cell number was monitored by manual cell counting over time as indicated. Unpaired t test was performed so that ns $p > 0.05$.

(C) H720/MEKDD was transduced with gRNAs against HES1 (n = 2) and NTC (n = 1) and stable knockouts produced. Western blot was performed to validate efficient knockdown. MEKDD, total and phosphorylated ERK1/2, INSM1, ASCL1 are shown with Vinculin used as loading control.

(D) H720/MEKDD was transduced with Cas9 and gRNAs against JAG1 (n = 3, ±SEM) and NTC (n = 1, ±SEM). Following transduction with gRNAs, cell number was monitored by manual cell counting over time as indicated. Unpaired t test was performed so that ns $p > 0.05$.

(E) H720/MEKDD was transduced with gRNAs against JAG1 (n = 3) and no guide (n = 1) and stable knockouts were produced. Western blot was performed to validate efficient knockdown of JAG1. MEKDD, total and phosphorylated ERK1/2, INSM1, ASCL1 are shown with Vinculin used as loading control. JAG1 gRNAs were run on the same blot as NTC but cropped for visualization purposes.

DISCUSSION

The striking difference in the prevalence of MAPK alterations between NSCLC and SCLC is intriguing, particularly in light of the highly aggressive nature of SCLC. Limited research has gone into studying this observation, highlighting major knowledge gaps in understanding the role of this primary oncogenic signaling pathway in SCLC. Here, we focused on disentangling the MAPK pathway and its highly interconnected network of signaling pathways in SCLC.

We identified a subset of SCLC, comprised exclusively of SCLC-A models, that was selectively sensitive to MAPK activation *in vitro* and *in vivo* and showed strong upregulation of ERK negative feedback regulators DUSP6 and SPRY2 and the STAT signaling pathway through STAT3 (S727) upon MAPK activation. It was previously shown that Raf-activated human medullary thyroid cancer cells produce the autocrine-paracrine leukemia inhibitory factor, which subsequently activates the JAK-STAT3 pathway via phosphorylation on STAT3 (tyrosine 705 and serine 727) (Park et al., 2003). This autocrine-paracrine pathway was also active

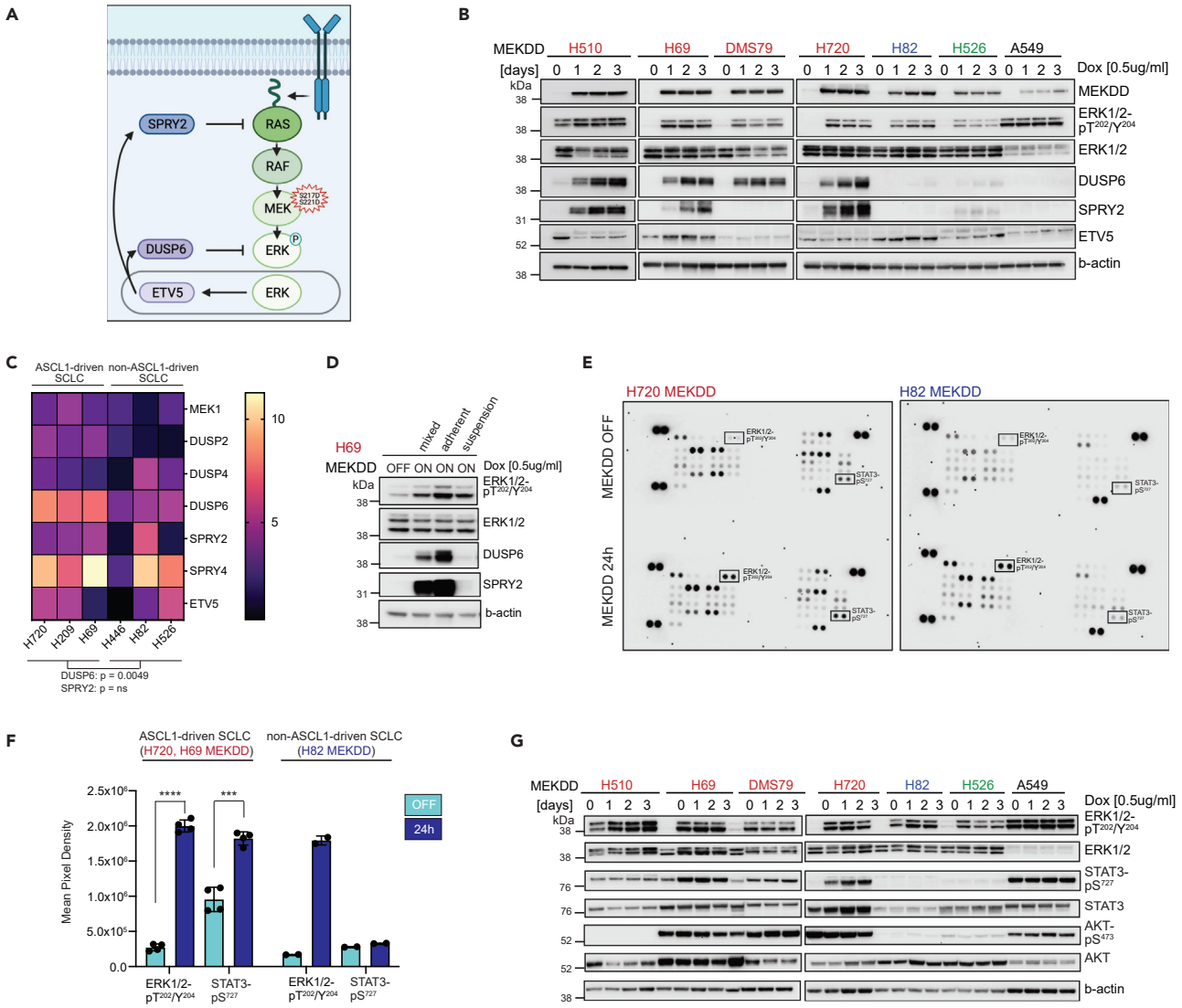

Figure 4. MAPK activation increases ERK negative feedback and activates STAT3

(A) A simplified schematic showing the MAPK pathway and its negative feedback regulators DUSP6, SPRY2, and ETV5. Created with BioRender.com.

(B) Western blot analysis on SCLC cell lines as indicated upon MEKDD$^{S217D/S221D}$ expression (0, 1, 2, 3 days). MEKDD, total and phosphorylated ERK1/2, DUSP6, SPRY2, ETV5 are shown with β-actin used as loading control. MEKDD, total and phosphorylated ERK1/2 were taken from Figure 1D for presentation purposes.

(C) Heatmap of SCLC cell lines showing log2 fold change for relative change in gene expression after MEKDD$^{S217D/S221D}$ expression (24 h) for the indicated genes. Unpaired t test was performed between ASCL1- and non-ASCL1-SCLC cell lines with p value as indicated.

(D) Western blot analysis on ASCL1-driven SCLC cell line H69 cultured as adherent, suspension, and mixed upon MEKDD$^{S217D/S221D}$ expression. Total and phosphorylated ERK1/2, DUSP6, and SPRY2 are shown with β-actin used as loading control. Total and phosphorylated ERK1/2 were taken from Figure 2C for presentation purposes.

(E) Phosphokinase array in H720 and H82 upon MEKDD$^{S217D/S221D}$ expression after 24 h. Phosphorylated ERK1/2 (T202/Y204) and STAT3 (S727) are indicated.

(F) Mean pixel density derived from (D) for phosphorylated ERK1/2 (T202/Y204) and STAT3 (S727) after 24 h of MEKDD$^{S217D/S221D}$ expression in the indicated cell lines (±SEM). Unpaired t test was performed so that ***$p < 0.001$, ****$p < 0.0001$.

(G) Western blot analysis on SCLC cell lines as indicated upon MEKDD$^{S217D/S221D}$ expression (0, 1, 2, 3 days). Total and phosphorylated ERK1/2, total and phosphorylated STAT3, and total and phosphorylated AKT are shown with β-actin used as loading control. Total and phosphorylated ERK1/2 were taken from Figure 2B for presentation purposes.

in two small cell lung cancer cell lines, yet at the time no subtype classification existed (Park et al., 2003). Here, we describe subtype specificity in regards to MAPK pathway tolerance and suggest that patients with SCLC-A-predominant tumors could benefit from tumor-specific MAPK activation.

Phenotypic changes were also distinct between SCLC subtypes. SCLC-A cell lines underwent macroscopic changes upon MAPK activation (apart from H720). This was most prominent in SCLC-A H69 that almost fully changed from suspension to adherent cells. This was accompanied by a decrease in NE markers and increase in EMT markers in the adherent cell population. This was not observed in the non-SCLC-A cell lines, suggesting a potential EMT phenotype specific to the ASCL1 subtype. Slight morphological changes were also seen in the H510 *in vivo* model (based on H&E), but this change was not as obvious as seen *in vitro*. We believe the overt microenvironmental differences between tissue culture and 3-dimensional tumor growth with stromal support can account for the distinction between *in vitro* and *in vivo* tumor morphologies.

Hyperactivation of oncogenes (e.g., RAS or BRAF) can cause oncogene-induced senescence, thereby limiting tumor development (Courtois-Cox et al., 2006). It is believed that the cause of oncogene-induced senescence is not hyperactive RAS signaling itself but rather upregulation of negative feedback pathways (e.g., RasGEFs, Sprouty proteins, RasGAPs, and DUSPs) (Courtois-Cox et al., 2006). Consistent with this model, we also observed an increase in ERK negative feedback regulators DUSP6 and SPRY2 upon MAPK activation in SCLC-A. It has previously been reported that primary samples from patients with pre-B ALL had higher protein expression of DUSP6, ETV5, and SPRY2 and were sensitive to DUSP6 inhibition (Shojaee et al., 2015). Similarly, small molecule inhibition of PTEN, negative regulator of the PI3K pathway, also proved to be toxic in pre-B ALL cells (Shojaee et al., 2016). It is thought that blocking negative feedback regulators pushes signaling above the maximum threshold resulting in cell death. Current treatment strategies focus on inhibiting oncogenic signaling so activation of oncogenic signaling might seem counterintuitive and also risks that patients potentially develop new cancers. Hence, we are cautious to propose the use of drugs that activate the MAPK pathway in patients with SCLC-A tumors.

To this date, limited research has gone into studying the MAPK pathway in SCLC (Cristea et al., 2020; Cristea and Sage, 2016; Falco et al., 1990; Park et al., 2003; Ravi et al., 1998, 1999). Although our study and others (Ravi et al., 1998, 1999) suggest MAPK pathway activity to be detrimental in SCLC tumors, others have argued that activation of the MAPK pathway may promote survival of some SCLC lines (Cristea et al., 2020; Cristea and Sage, 2016). These somewhat paradoxical observations suggest that MAPK signaling in SCLC is highly context dependent. MAPK pathway activation may occur through several mechanisms such as alterations in genes of the MAPK pathway as well as its negative regulators, signaling through receptor tyrosine kinases, or G-protein-coupled receptors. The resulting signal intensity may differ across mechanisms, resulting in toxicity to tumor cells in some contexts and oncogenesis in others. The signal intensity and downstream consequences also differ between SCLC subtypes, suggesting that the optimal therapy may be dependent on the underlying SCLC subtype.

This study has unveiled certain similarities in regards to signaling between SCLC-A and hematological malignancies. In fact, Balanis et al. (2019) report that small-cell neuroendocrine cancers and hematological cancers share gene and protein expression profiles: hematological cancers had protein profiles highly similar to SCLC, whereas SCLC and LUAD cell lines were well segregated. Of interest, small-cell neuroendocrine and hematological cancers also shared drug sensitivities (Balanis et al., 2019). These observations suggest that it might be beneficial to test therapeutic approaches successful in hematological malignancies also in SCLC and *vice versa*.

This study provides additional understanding of SCLC biology, in particular regarding its complex signaling networks including interactions between MAPK and STAT3 pathways. It presents the first experiments suggesting that a certain subtype of SCLC only tolerates low MAPK activity. These data may provide insight into SCLC dependencies and potential subtype-specific drug susceptibilities.

Limitations of the study

We would like to acknowledge the following caveats in this study. First, SCLC cell lines mostly grow in clusters in suspension, which made it technically difficult to use the conventional senescence assay with β-galactosidase Staining Kit. Although viewed as the "gold standard" to study senescence, it is not optimized for suspension cells. We therefore took advantage of using a fluorescent, and not colorimetric, substrate for β-gal for the detection of senescent cells that can easily be quantified on a flow cytometer.

Second, directly comparing the expression of signaling pathways in cells grown *in vitro* to cells grown *in vivo* may be misleading owing to the distinct microenvironment in these settings. The *in vivo* models in this

study were created by injecting cells resuspended in Matrigel, an extracellular matrix mixture. For cells to engraft in this *in vivo* setting, different pathways may have to be upregulated, which might not be needed when cells are grown in a flask. We may therefore observe slight differences in the signaling expression levels *in vitro* versus *in vivo* such as the phosphorylation of ERK.

Third, to determine whether deletion of NOTCH target genes would reverse the effects induced by MAPK activation such as growth inhibition, we chose a proliferation assay as the major readout owing to proliferation being integrally connected to tumor progression. This was based on our *in vivo* experiments where MAPK-induced decrease in cell viability resulted in longer survival and smaller tumor volumes. It would also be interesting to determine any cellular macroscopic changes upon deletion of NOTCH target genes following MAPK activation, as well as identify whether NOTCH target gene deletion results in a switch in morphology when these cells are injected *in vivo*, although this is outside the scope of this study.

Finally, the results presented here could be further confirmed in a larger cohort of *in vivo* models representing different SCLC subtypes and determining potential therapeutic susceptibilities for ASCL1-driven SCLC, although again this is outside the scope of this study.

STAR★METHODS

Detailed methods are provided in the online version of this paper and include the following:

- KEY RESOURCES TABLE
- RESOURCE AVAILABILITY
  - Lead contact
  - Materials availability
  - Data and code availability
- EXPERIMENTAL MODEL AND SUBJECT DETAILS
  - Cell culture and cell lines
  - Mouse models
- METHOD DETAILS
  - Plasmids
  - Western Blot
  - Cell viability assay
  - Chemicals
  - Mouse studies
  - Annexin V/DAPI apoptosis assay
  - Click-iT Edu cell cycle analysis
  - Cell senescence analysis
  - Lentiviral production and transduction
  - Generation of doxycycline-inducible MEKDD$^{S217D/S221D}$ (MEK1) cell lines
  - Phosphokinase array
  - Cell images
  - RNA extraction, sequencing, and analysis RNA_seq analysis
  - Histology
  - CRISPR/Cas9
- QUANTIFICATION AND STATITICAL ANALYSIS

SUPPLEMENTAL INFORMATION

Supplemental information can be found online at https://doi.org/10.1016/j.isci.2021.103224.

ACKNOWLEDGMENTS

Supported by NCI R01 CA258784 (T.S.), NCI R01 CA197936 and U24 CA213274 (C.M.R.), the SU2C/VAI Epigenetics Dream Team (C.M.R.), NCI R35 CA263816 (C.M.R.), the Druckenmiller Center for Lung Cancer Research (C.M.R., T.S.), Parker Institute for Cancer Immunotherapy grant (T.S.); International Association for the Study of Lung Cancer grant (T.S.). We acknowledge the use of the Integrated Genomics Operation Core, funded by the NCI Cancer Center Support Grant (CCSG, P30 CA08748), Cycle for Survival, and the Marie-Josée and Henry R. Kravis Center for Molecular Oncology and the National Cancer Institute Cancer Center Core Grant No. P30-CA008748. The PPBC Biobank and Precision Pathology Center are supported

by the NCI Cancer Center Support Grant P30-CA008748. We gratefully acknowledge the members of the Molecular Diagnostics Service in the Department of Pathology. We thank all members of the MSKCC Antitumor Assessment Core Facility (core grant: P30 CA008748 S5). We thank all members of the Flow Cytometry Core Facility, especially Kathleen Daniels, for training and assistance. We thank all members of the Rudin laboratory for their collaborative efforts.

AUTHOR CONTRIBUTIONS

Conceptualization: R.C., C.H, C.M.R., T.S.; methodology: R.C., C.H., E.C., V.D., N.S.S., M.L., X.C., S.S.C., S.E.T., M.C., E.d.S., J.T.P., M.A., F.E.K., C.M.R., T.S.; investigation: R.C., C.H., T.S., C.M.R.; validation: R.C.; formal analysis: R.C., C.H., E.C., S.S.C., C.M.R., T.S.; writing: R.C., T.S., C.M.R.; supervision: T.S. and C.M.R.; funding acquisition: T.S. and C.M.R. All authors read and approved the final version of the manuscript.

DECLARATION OF INTERESTS

C.M.R. has consulted regarding oncology drug development with Amgen, Daiichi Sankyo, Genentech/Roche, Ipsen, Jazz, Merck, Pfizer, Syros, and Vavotek. C.M.R. serves on the scientific advisory boards of Bridge Medicines, Earli, and Harpoon Therapeutics.

Received: April 9, 2021
Revised: August 2, 2021
Accepted: September 30, 2021
Published: November 19, 2021

REFERENCES

Baine, M.K., Hsieh, M.S., Lai, W.V., Egger, J.V., Jungbluth, A.A., Daneshbod, Y., Beras, A., Spencer, R., Lopardo, J., Bodd, F., and Montecalvo, J. (2020). SCLC subtypes defined by ASCL1, NEUROD1, POU2F3, and YAP1: a comprehensive immunohistochemical and histopathologic characterization. J. Thorac. Oncol. *15*, 1823–1835. https://doi.org/10.1016/j.jtho.2020.09.009.

Balanis, N.G., Sheu, K.M., Esedebe, F.N., Patel, S.J., Smith, B.A., Park, J.W., Alhani, S., Gomperts, B.N., Huang, J., Witte, O.N., and Graeber, T.G. (2019). Pan-cancer convergence to a small-cell neuroendocrine phenotype that shares susceptibilities with hematological malignancies. Cancer Cell *36*, 17–34.e17. https://doi.org/10.1016/j.ccell.2019.06.005.

Bernhardt, E.B., and Jalal, S.I. (2016). Small cell lung cancer. Cancer Treat. Res. *170*, 301–322. https://doi.org/10.1007/978-3-319-40389-2_14.

Borges, M., Linnoila, R.I., Van De Velde, H.J., Chen, H., Nelkin, B.D., Mabry, M., Baylin, S.B., and Ball, D.W. (1997). An achaete-scute homologue essential for neuroendocrine differentiation in the lung. Nature *386*, 852–855. https://doi.org/10.1038/386852a0.

Borromeo, M.D., Savage, T.K., Kollipara, R.K., He, M., Augustyn, A., Osborne, J.K., Girard, L., Minna, J.D., Gazdar, A.F., Cobb, M.H., and Johnson, J.E. (2016). ASCL1 and NEUROD1 reveal heterogeneity in pulmonary neuroendocrine tumors and regulate distinct genetic programs. Cell Rep. *16*, 1259–1272. https://doi.org/10.1016/j.celrep.2016.06.081.

Byers, L.A., and Rudin, C.M. (2015). Small cell lung cancer: where do we go from here? Cancer *121*, 664–672. https://doi.org/10.1002/cncr.29098.

Byers, L.A., Wang, J., Nilsson, M.B., Fujimoto, J., Saintigny, P., Yordy, J., Giri, U., Peyton, M., Fan, Y.H., Diao, L., and Masrorpour, F. (2012). Proteomic profiling identifies dysregulated pathways in small cell lung cancer and novel therapeutic targets including PARP1. Cancer Discov. *2*, 798–811. https://doi.org/10.1158/2159-8290.CD-12-0112.

Calbo, J., van Montfort, E., Proost, N., van Drunen, E., Beverloo, H.B., Meuwissen, R., and Berns, A. (2011). A functional role for tumor cell heterogeneity in a mouse model of small cell lung cancer. Cancer Cell *19*, 244–256. https://doi.org/10.1016/j.ccr.2010.12.021.

Cerami, E., Gao, J., Dogrusoz, U., Gross, B.E., Sumer, S.O., Aksoy, B.A., Jacobsen, A., Byrne, C.J., Heuer, M.L., Larsson, E., and Antipin, Y. (2012). The cBio cancer genomics portal: an open platform for exploring multidimensional cancer genomics data. Cancer Discov. *2*, 401–404. https://doi.org/10.1158/2159-8290.CD-12-0095.

Cheng, D.T., Mitchell, T.N., Zehir, A., Shah, R.H., Benayed, R., Syed, A., Chandramohan, R., Liu, Z.Y., Won, H.H., Scott, S.N., and Brannon, A.R. (2015). Memorial sloan kettering-integrated mutation profiling of actionable cancer targets (MSK-IMPACT): a hybridization capture-based next-generation sequencing clinical assay for solid tumor molecular oncology. J. Mol. Diagn. *17*, 251–264. https://doi.org/10.1016/j.jmoldx.2014.12.006.

Courtois-Cox, S., Williams, S.M.G., Reczek, E.E., Johnson, B.W., McGillicuddy, L.T., Johannessen, C.M., Hollstein, P.E., MacCollin, M., and Cichowski, K. (2006). A negative feedback signaling network underlies oncogene-induced senescence. Cancer Cell *10*, 459–472. https://doi.org/10.1016/j.ccr.2006.10.003.

Cristea, S., Coles, G.L., Hornburg, D., Gershkovitz, M., Arand, J., Cao, S., Sen, T., Williamson, S.C., Kim, J.W., Drainas, A.P., and He, A. (2020). The MEK5-ERK5 kinase axis controls lipid metabolism in small-cell lung cancer. Cancer Res. *80*, 1293–1303. https://doi.org/10.1158/0008-5472.CAN-19-1027.

Cristea, S., and Sage, J. (2016). Is the canonical RAF/MEK/ERK signaling pathway a therapeutic target in SCLC? J. Thorac. Oncol. *11*, 1233–1241. https://doi.org/10.1016/j.jtho.2016.04.018.

Falco, J.P., Baylin, S.B., Lupu, R., Borges, M., Nelkin, B.D., Jasti, R.K., Davidson, N.E., and Mabry, M. (1990). v-rasH induces non-small cell phenotype, with associated growth factors and receptors, in a small cell lung cancer cell line. J. Clin. Invest. *85*, 1740–1745. https://doi.org/10.1172/JCI114630.

Gao, J., Aksoy, B.A., Dogrusoz, U., Dresdner, G., Gross, B., Sumer, S.O., Sun, Y., Jacobsen, A., Sinha, R., Larsson, E., and Cerami, E. (2013). Integrative analysis of complex cancer genomics and clinical profiles using the cBioPortal. Sci. Signal *6*, pl1. https://doi.org/10.1126/scisignal.2004088.

Gay, C.M., Stewart, C.A., Park, E.M., Diao, L., Groves, S.M., Heeke, S., Nabet, B.Y., Fujimoto, J., Solis, L.M., Lu, W., and Xi, Y. (2021). Patterns of transcription factor programs and immune pathway activation define four major subtypes of SCLC with distinct therapeutic vulnerabilities. Cancer Cell *39*, 346–360.e347. https://doi.org/10.1016/j.ccell.2020.12.014.

George, J., Lim, J.S., Jang, S.J., Cun, Y., Ozretić, L., Kong, G., Leenders, F., Lu, X., Fernández-Cuesta, L., Bosco, G., and Müller, C. (2015). Comprehensive genomic profiles of small cell

lung cancer. Nature *524*, 47–53. https://doi.org/10.1038/nature14664.

Hann, C., Wu, M.A., Rekhtman, N., and Rudin, C.M. (2019). Small cell and neuroendocrine tumors of the lung. In Cancer Principles & Practice of Oncology, V.T. DeVita, T.S. Lawrence, and S.A. Rosenberg, eds. (Wolters Kluwer).

Horn, L., Mansfield, A.S., Szczęsna, A., Havel, L., Krzakowski, M., Hochmair, M.J., Huemer, F., Losonczy, G., Johnson, M.L., Nishio, M., and Reck, M. (2018). First-line atezolizumab plus chemotherapy in extensive-stage small-cell lung cancer. N. Engl. J. Med. *379*, 2220–2229. https://doi.org/10.1056/NEJMoa1809064.

Lim, J.S., Ibaseta, A., Fischer, M.M., Cancilla, B., O'Young, G., Cristea, S., Luca, V.C., Yang, D., Jahchan, N.S., Hamard, C., and Antoine, M. (2017). Intratumoural heterogeneity generated by Notch signalling promotes small-cell lung cancer. Nature *545*, 360–364. https://doi.org/10.1038/nature22323.

Meerbrey, K.L., Hu, G., Kessler, J.D., Roarty, K., Li, M.Z., Fang, J.E., Herschkowitz, J.I., Burrows, A.E., Ciccia, A., Sun, T., and Schmitt, E.M.((2011). The pINDUCER lentiviral toolkit for inducible RNA interference in vitro and in vivo. Proc. Natl. Acad. Sci. U. S. A. *108*, 3665–3670. https://doi.org/10.1073/pnas.1019736108.

Michaloglou, C., Vredeveld, L.C., Soengas, M.S., Denoyelle, C., Kuilman, T., Van Der Horst, C.M., Majoor, D.M., Shay, J.W., Mooi, W.J., and Peeper, D.S. (2005). BRAFE600-associated senescence-like cell cycle arrest of human naevi. Nature *436*, 720–724. https://doi.org/10.1038/nature03890.

Owonikoko, T.K., Dwivedi, B., Chen, Z., Zhang, C., Barwick, B., Ernani, V., Zhang, G., Gilbert-Ross, M., Carlisle, J., Khuri, F.R., and Curran, W.J. (2021). YAP1 expression in SCLC defines a distinct subtype with T-cell-inflamed phenotype. J. Thorac. Oncol. *16*, 464–476. https://doi.org/10.1016/j.jtho.2020.11.006.

Park, J.I., Strock, C.J., Ball, D.W., and Nelkin, B.D. (2003). The Ras/Raf/MEK/extracellular signal-regulated kinase pathway induces autocrine-paracrine growth inhibition via the leukemia inhibitory factor/JAK/STAT pathway. Mol. Cell Biol. *23*, 543–554. https://doi.org/10.1128/MCB.23.2.543-554.2003.

Paz-Ares, L., Dvorkin, M., Chen, Y., Reinmuth, N., Hotta, K., Trukhin, D., Statsenko, G., Hochmair, M.J., Özgüroğlu, M., Ji, J.H., and Voitko, O. (2019). Durvalumab plus platinum-etoposide versus platinum-etoposide in first-line treatment of extensive-stage small-cell lung cancer (CASPIAN): a randomised, controlled, open-label, phase 3 trial. Lancet *394*, 1929–1939. https://doi.org/10.1016/S0140-6736(19)32222-6.

Pearsall, S.M., Humphrey, S., Revill, M., Morgan, D., Frese, K.K., Galvin, M., Kerr, A., Carter, M., Priest, L., Blackhall, F., and Simpson, K.L. (2020). The rare YAP1 subtype of SCLC revisited in a biobank of 39 circulating tumor cell patient derived explant models: a brief report. J. Thorac. Oncol. *15*, 1836–1843. https://doi.org/10.1016/j.jtho.2020.07.008.

Peifer, M., Fernández-Cuesta, L., Sos, M.L., George, J., Seidel, D., Kasper, L.H., Plenker, D., Leenders, F., Sun, R., Zander, T., and Menon, R. (2012). Integrative genome analyses identify key somatic driver mutations of small-cell lung cancer. Nat. Genet. *44*, 1104–1110. https://doi.org/10.1038/ng.2396.

Perez, A.R., Pritykin, Y., Vidigal, J.A., Chhangawala, S., Zamparo, L., Leslie, C.S., and Ventura, A. (2017). GuideScan software for improved single and paired CRISPR guide RNA design. Nat. Biotechnol. *35*, 347–349. https://doi.org/10.1038/nbt.3804.

Poirier, J.T., George, J., Owonikoko, T.K., Berns, A., Brambilla, E., Byers, L.A., Carbone, D., Chen, H.J., Christensen, C.L., Dive, C., and Farago, A.F. (2020). New approaches to SCLC therapy: from the laboratory to the clinic. J. Thorac. Oncol. *15*, 520–540. https://doi.org/10.1016/j.jtho.2020.01.016.

Ravi, R.K., Thiagalingam, A., Weber, E., McMahon, M., Nelkin, B.D., and Mabry, M. (1999). Raf-1 causes growth suppression and alteration of neuroendocrine markers in DMS53 human small-cell lung cancer cells. Am. J. Respir. Cell Mol. Biol. *20*, 543–549. https://doi.org/10.1165/ajrcmb.20.4.3406.

Ravi, R.K., Weber, E., McMahon, M., Williams, J.R., Baylin, S., Mal, A., Harter, M.L., Dillehay, L.E., Claudio, P.P., Giordano, A., and Nelkin, B.D. (1998). Activated Raf-1 causes growth arrest in human small cell lung cancer cells. J. Clin. Invest. *101*, 153–159. https://doi.org/10.1172/JCI831.

Rudin, C.M., Awad, M.M., Navarro, A., Gottfried, M., Peters, S., Csőszi, T., Cheema, P.K., Rodriguez-Abreu, D., Wollner, M., Yang, J.C.H., and Mazieres, J. (2020). Pembrolizumab or placebo plus etoposide and platinum as first-line therapy for extensive-stage small-cell lung cancer: randomized, double-blind, phase III KEYNOTE-604 study. J. Clin. Oncol. *38*, 2369–2379. https://doi.org/10.1200/JCO.20.00793.

Rudin, C.M., Brambilla, E., Faivre-Finn, C., and Sage, J. (2021). Small-cell lung cancer. Nat. Rev. Dis. Primers *7*, 3. https://doi.org/10.1038/s41572-020-00235-0.

Rudin, C.M., Durinck, S., Stawiski, E.W., Poirier, J.T., Modrusan, Z., Shames, D.S., Bergbower, E.A., Guan, Y., Shin, J., Guillory, J., and Rivers, C.S. (2012). Comprehensive genomic analysis identifies SOX2 as a frequently amplified gene in small-cell lung cancer. Nat. Genet. *44*, 1111–1116. https://doi.org/10.1038/ng.2405.

Rudin, C.M., Poirier, J.T., Byers, L.A., Dive, C., Dowlati, A., George, J., Heymach, J.V., Johnson, J.E., Lehman, J.M., MacPherson, D., and Massion, P.P. (2019). Molecular subtypes of small cell lung cancer: a synthesis of human and mouse model data. Nat. Rev. Cancer *19*, 289–297. https://doi.org/10.1038/s41568-019-0133-9.

Sanjana, N.E., Shalem, O., and Zhang, F. (2014). Improved vectors and genome-wide libraries for CRISPR screening. Nat. Methods *11*, 783–784. https://doi.org/10.1038/nmeth.3047.

Schubbert, S., Shannon, K., and Bollag, G. (2007). Hyperactive Ras in developmental disorders and cancer. Nat. Rev. Cancer *7*, 295–308. https://doi.org/10.1038/nrc2109.

Serrano, M., Lin, A.W., McCurrach, M.E., Beach, D., and Lowe, S.W. (1997). Oncogenic ras provokes premature cell senescence associated with accumulation of p53 and p16INK4a. Cell *88*, 593–602. https://doi.org/10.1016/s0092-8674(00)81902-9.

Shieh, A., Ward, A.F., Donlan, K.L., Harding-Theobald, E.R., Xu, J., Mullighan, C.G., Zhang, C., Chen, S.C., Su, X., Downing, J.R., and Bollag, G.E. (2013). Defective K-Ras oncoproteins overcome impaired effector activation to initiate leukemia in vivo. Blood *121*, 4884–4893. https://doi.org/10.1182/blood-2012-05-432252.

Shojaee, S., Caeser, R., Buchner, M., Park, E., Swaminathan, S., Hurtz, C., Geng, H., Chan, L.N., Klemm, L., Hofmann, W.K., and Qiu, Y.H.((2015). Erk negative feedback control enables pre-B cell transformation and represents a therapeutic target in acute lymphoblastic leukemia. Cancer Cell *28*, 114–128. https://doi.org/10.1016/j.ccell.2015.05.008.

Shojaee, S., Chan, L.N., Buchner, M., Cazzaniga, V., Cosgun, K.N., Geng, H., Qiu, Y.H., Von Minden, M.D., Ernst, T., Hochhaus, A., and Cazzaniga, G. (2016). PTEN opposes negative selection and enables oncogenic transformation of pre-B cells. Nat. Med. *22*, 379–387. https://doi.org/10.1038/nm.4062.

Sriuranpong, V., Borges, M.W., Ravi, R.K., Arnold, D.R., Nelkin, B.D., Baylin, S.B., and Ball, D.W. (2001). Notch signaling induces cell cycle arrest in small cell lung cancer cells. Cancer Res. *61*, 3200–3205. https://www.ncbi.nlm.nih.gov/pubmed/11306509.

Tremblay, I., Pare, E., Arsenault, D., Douziech, M., and Boucher, M.J. (2013). The MEK/ERK pathway promotes NOTCH signalling in pancreatic cancer cells. PLoS One *8*, e85502. https://doi.org/10.1371/journal.pone.0085502.

Wagle, M.C., Kirouac, D., Klijn, C., Liu, B., Mahajan, S., Junttila, M., Moffat, J., Merchant, M., Huw, L., Wongchenko, M., and Okrah, K. (2018). A transcriptional MAPK Pathway Activity Score (MPAS) is a clinically relevant biomarker in multiple cancer types. NPJ Precis Oncol. *2*, 7. https://doi.org/10.1038/s41698-018-0051-4.

Wohlhieter, C.A., Richards, A.L., Uddin, F., Hulton, C.H., Quintanal-Villalonga, À., Martin, A., de Stanchina, E., Bhanot, U., Asher, M., Shah, N.S., and Hayatt, O. (2020). Concurrent mutations in STK11 and KEAP1 promote ferroptosis protection and SCD1 dependence in lung cancer. Cell Rep. *33*, 108444. https://doi.org/10.1016/j.celrep.2020.108444.

Yu, R.T.D., and Garcia, R.L. (2020). NRAS mutant E132K identified in young-onset sporadic colorectal cancer and the canonical mutants G12D and Q61K affect distinct oncogenic phenotypes. Sci. Rep. *10*, 11028. https://doi.org/10.1038/s41598-020-67796-8.

STAR★METHODS

KEY RESOURCES TABLE

REAGENT or RESOURCE	SOURCE	IDENTIFIER
Antibodies		
Beta-actin	Cell Signalling	Cat#4967; RRID: AB_2198872
DUSP6	Abcam	Cat#ab76310; RRID:AB_1523517
ERK1/2	Cell Signalling	Cat#9102; RRID: AB_330744
Phospho -ERK1/2 (T202/Y204)	Cell Signalling	Cat#4370; RRID: AB_2315112
ETV5	Proteintech	Cat#13011-1-AP; RRID: AB_2278092
SPRY2	Cell Signalling	Cat#14954; RRID: AB_2798658
HA-Tag for Phospho-MEK1/2 (Ser217/221)	Cell Signalling	Cat# 3724; RRID: AB_1549585
NEUROD1	Santa Cruz	Cat#sc-46684; RRID: AB_671759
POU2F3	Santa Cruz	Cat#sc-293402; RRID: AB_2890011
Anti-MASH1 (ASCL1)	BD Pharmingen	Cat#556604; RRID: AB_396479
INSM1	Santa Cruz	Cat#sc-271408; RRID: AB_10607955
Synaptophysin (SYP)	Neuromics	Cat#MO20000; RRID: AB_2198872
E-cadherin	Cell Signalling	Cat#3195; RRID: AB_2291471
N-Cadherin	Cell Signalling	Cat#13116; RRID: AB_2687616
Vimentin	Cell Signalling	CAT#5741; RRID: AB_10695459
NOTCH2	Cell Signalling	CAT#5732; RRID: AB_10693319
NOTCH1	Cell Signalling	CAT#4380; RRID: AB_10691684
Vinculin	Cell Signalling	CAT#13901; RRID: AB_2714181
Phospho-Stat3 (Ser727)	Cell Signalling	CAT#9134; RRID: AB_331589
Stat3	Cell Signalling	CAT#4904; RRID: AB_331269
Cleaved NOTCH1	Cell Signalling	CAT#4147; RRID: AB_2153348
P27	Cell Signalling	CAT#3686; RRID: AB_2077850
HES1	Cell Signalling	CAT#11988; RRID: AB_2728766
Jagged1	Cell Signalling	CAT#2620; RRID: AB_10693295
Chemicals, peptides, and recombinant proteins		
Z-VAD-FMK	Promega	CAT#G7231
Doxycycline Hydrochloride	Thermo Fisher Scientific	CAT#BP26531
Critical commercial assays		
Click-iT™ EdU Alexa Fluor™ 488 Flow Cytometry Assay Kit	Thermo Fisher	CAT#C10425
CellEvent™ Senescence Green Flow Cytometry Assay Kit	Thermo Fisher	CAT#C10840
Proteome Profiler Human Phospho-Kinase Array Kit	R&D	CAT#ARY003C
Deposited data		
Raw RNAseq data	This paper	ArrayExpress: E-MTAB-11016
Experimental models: Cell lines		
H720	ATCC	CAT#CRL-5838; RRID: CVCL_1583
H69	ATCC	CAT#HTB-119; RRID: CVCL_1579
DMS79	ATCC	CAT#CRL-2049; RRID: CVCL_1178
H510	ATCC	CAT#HTB-184; RRID: CVCL_1565
H82	ATCC	CAT#HTB-175; RRID: CVCL_1591
H526	ATCC	CAT#CRL-5811; RRID: CVCL_1569

(*Continued on next page*)

Continued

REAGENT or RESOURCE	SOURCE	IDENTIFIER
A549	ATCC	CAT#CCL-185; RRID: CVCL_0023
H209	ATCC	CAT#HTB-172; RRID: CVCL_1525
H128	ATCC	CAT#HTB-120; RRID: CVCL_1460
H446	ATCC	CAT#HTB-171; RRID: CVCL_1562
H460	ATCC	CAT#HTB-177; RRID: CVCL_0459
H292	ATCC	CAT#CRL-1848; RRID: CVCL_0455
H661	ATCC	CAT#HTB-183; RRID: CVCL_1577
H522	ATCC	CAT#CRL-5810; RRID: CVCL_1567
Experimental models: Organisms/strains		
Mouse: athymic *nude* females, 6-8 weeks old	ENVIGO	NA
Oligonucleotides		
plentiCRISPRv2/HES1_1: GGTATTAACGCCCTCGCACG	This paper	NA
plentiCRISPRv2/HES1_2: ATCAATGCCATGACCTACCC	This paper	NA
plentiCRISPRv2/JAG1_1: ATGGGCCCCGAATGTAACAG	This paper	NA
plentiCRISPRv2/JAG1_2: AAGTGCAAGAGTCAGTCGGG	This paper	NA
plentiCRISPRv2/JAG1_3: CGCGGGACTGATACTCCTTG	This paper	NA
plentiCRISPRv2/NTC: ACGGAGGCTAAGCGTCGCAA	This paper	NA
Recombinant DNA		
pInducer20	Addgene	RRID:Addgene_44012
Software and algorithms		
FlowJo	BD Biosciences	https://www.flowjo.com
MSK-IMPACT	Cheng et al., 2015	NA
cBioPortal	Cerami et al., 2012	http://www.cbioportal.org

RESOURCE AVAILABILITY

Lead contact

Further information and requests for resources and reagents should be directed to and will be fulfilled by the lead contact, Triparna Sen (sent@mskcc.org).

Materials availability

This study did not generate new unique reagents.

Data and code availability

- RNA seq data have been deposited at ArrayExpress: E-MTAB-11016 and are publicly available as of the date of publication. Accession numbers are listed in the key resources table.
- This paper does not report original code.
- Any additional information required to reanalyze the data reported in this paper is available from the lead contact upon request.

EXPERIMENTAL MODEL AND SUBJECT DETAILS

Cell culture and cell lines

The following cell lines were used in this study: H720 (ATCC CAT#CRL-5838; RRID: CVCL_1583), H69 (ATCC CAT#HTB-119; RRID: CVCL_1579), DMS79 (ATCC CAT#CRL-2049; RRID: CVCL_1178), H510 (ATCC CAT#HTB-184; RRID: CVCL_1565), H82 (ATCC CAT#HTB-175; RRID: CVCL_1591), H526 (ATCC CAT#CRL-5811; RRID: CVCL_1569), A549 (ATCC CAT#CCL-185; RRID: CVCL_0023), H209 (ATCC CAT#HTB-172; RRID: CVCL_1525), H128 (ATCC CAT#HTB-120; RRID: CVCL_1460), H446

(ATCC CAT#HTB-171; RRID: CVCL_1562), H460 (ATCC CAT#HTB-177; RRID: CVCL_0459), H292 (ATCC CAT#CRL-1848; RRID: CVCL_0455), H661 (ATCC CAT#HTB-183; RRID: CVCL_1577), H522 (ATCC CAT#CRL-5810; RRID: CVCL_1567). All cell lines apart from H510 were cultured in Roswell Park Memorial Institute medium (RPMI-1640, Invitrogen, Carlsbad, CA) containing 10% Tet-free FBS, 100 IU/ml penicillin and 100 μg/ml streptomycin and kept at 37°C in a humidified incubator (5% CO_2 and 95% atmosphere). H510 was cultured in Kaighn's Modification of Ham's F-12 Medium (F12-K, ATCC 20-2004) containing 10% Tet-free FBS, 100 IU/ml penicillin and 100 μg/ml streptomycin and kept at 37°C in a humidified incubator (5% CO_2 and 95% atmosphere). All cell lines used in this study are negative for mycoplasma contamination and were confirmed by STR profiling.

Lenti-X 293 T Cell Line (Clontech Laboratories, 632180) were cultured in Dulbecco's modified Eagle's medium (DMEM, Invitrogen, Carlsbad, CA) that contained 10% FBS, 100 IU/ml penicillin, and 100 μg/ml streptomycin and kept as above.

Mouse models

All animal experiments were approved by the Memorial Sloan Kettering Cancer Center (MSKCC) Animal Care and Use Committee. Female nude mice (6-8 weeks old) were obtained from Charles Rivers Laboratories and housed in accredited facilities under pathogen-free conditions. Additional information on experimental methods in next section.

METHOD DETAILS

Plasmids

The CDS for human gene sequences $MEKDD^{S217D/S221D}$ was cloned into BsrGI-cut pInducer20 backbone for the Tet-inducible expression of $MEKDD^{S217D/S221D}$. pInducer20 was a gift from Stephen Elledge (Addgene plasmid # 44012; http://n2t.net/addgene:44012; RRID:Addgene_44012 (Meerbrey et al., 2011). Capillary sequencing was used to verify plasmids.

Western Blot

Cell lysates were prepared from frozen cell pellets or flash frozen tumour samples as follows: CelLytic buffer (Sigma) supplemented with 1% protease inhibitor cocktail (Roche), 1% phosphatase inhibitor cocktail (Calbiochem Millipore) was used to lyse cells. The same amount of protein per sample was loaded on NuPAGE (Invitrogen) 4–12% Bis-Tris gradient gels and further transferred on PVDF membranes (Bio-Rad). To detect human proteins, the HRP immunodetection system (Millipore) and the iBright Western Blot Imaging System (ThermoFisher) were used.

Cell viability assay

Cells (H720, H82, H69, H526: 1500 cells/well; DMS79, H510: 2000 cells/well; A549: 1000 cells/well) were plated in a volume of 180ul in Falcon Clear 96-well plate (BD Biosciences). After >3h incubation at 37°C, doxycycline (0.5 μg/ml) was diluted in medium and added to the indicated wells and re-added every 2 days. After incubation for the indicated timepoint, CellTiter-Glo 2.0 Cell Viability Assay (Promega, G9241) was added to each well and luminescence measured according to manufacturer's instructions. Baseline values of untreated cells were used as a reference to calculate fold changes (set to 1).

Chemicals

Doxycycline Hydrochloride (Cat# BP26531) was purchased from FisherScientific (Hampton, NH, USA). Z-VAD-FMK (Cat# G7231) was purchased from Promega (Madison, WI).

Mouse studies

Cultured human SCLC cell lines were injected subcutaneously into the right flank of athymic nude female mice (6–8 weeks old) (ENVIGO). Up to 2×10^6 cells were washed and resuspended in Matrigel and PBS in a 1:1 ratio. Three days prior to injection until the end of experiment, mice in the doxycycline cohort were fed doxycycline chow. Tumor dimensions were analyzed using a caliper once to twice weekly and volume calculated using the equation $V = \pi/6*L*W^2$ (L length; W width). Tumors were harvested once tumor volume reached 1500 mm^3 and weights subsequently measured using a scale. Tumors were processed immediately after harvest and flash-frozen and submerged in formalin for further analysis. All animal experiments

were approved by the Memorial Sloan Kettering Cancer Center (MSKCC) Animal Care and Use Committee. Mice were housed in accredited facilities under pathogen-free conditions.

Annexin V/DAPI apoptosis assay

APC-Annexin V/Dead Cell Apoptosis Assay was used for the detection of apoptotic cells according to the manufacturer's instructions. Externalization of phosphatidylserine (Annexin V, APC Conjugate, Cat # 640919) and DNA content (DAPI, 4',6-diamidino-2-phenylindole, Cat# D9542) were measured on a Fortessa Flow Cytometer. Gating on all cells using FlowJo software was used for analysis.

Click-iT Edu cell cycle analysis

Click-iT™ EdU Alexa Fluor™ 488 Flow Cytometry Assay Kit (Thermo Fisher, C10425) was used for the analysis of DNA replication in proliferating cells according to manufacturer's instructions. Click-iT EdU labeling (Alexa Fluor 488 Conjugate) and DNA content (DAPI, 4',6-diamidino-2-phenylindole) were measured on a Fortessa Flow Cytometer and further analyzed using FlowJo software.

Cell senescence analysis

CellEvent™ Senescence Green Flow Cytometry Assay Kit (Thermo Fisher, C10840) was used for the analysis of cellular senescence via β -galactosidase hydrolysis according to manufacturer's instructions. Activation of β -galactosidase (emitting a fluorogenic signal detected on 488 laser) was measured on a Fortessa Flow Cytometer.

Lentiviral production and transduction

Lentiviral packaging plasmids psPAX2 (Addgene plasmid #12260, gift from Didier Trono http://n2t.net/addgene:12260; RRID:Addgene_12260) and pMD.2G (Addgene plasmid # 12259, gift from Didier Trono http://n2t.net/addgene:12259; RRID:Addgene_12259) were used as follows: 8.33μg psPAX2 (gag-pol) and 4.12μg pMD.2G (envelope) and 12.5μg of lentiviral construct were used to transfect a 15cm dish of Lenti-X 293T cell line, after mixing with 1ml of Jet Buffer and 50μl of JetPRIME reagent. Media was changed 16 hours post transfection and supernatant filtered through a 0.45μM filter 72h post transfection. Supernatant was concentrated using Lenti-X Concentrator (Fisher Scientific, NC0448638) according to manufacturer's instructions. Virus was resuspended in 500μl DMEM media (20 x concentrated) and stored at −80°C. For lentiviral transduction, 0.5×10^6 cells were resuspended in 1ml media and 2 μl Polybrene (8 mg/ml) and mixed with 300μl concentrated virus. Following incubation at 37°C for 10min, cells were infected by centrifugation (800 g, 30min) in a 12-well plate. Cells were selected for pInducer20/MEKDD using Neomycin (G418) (200–800 μg/ml) every 2–3 days until control cells are dead.

Generation of doxycycline-inducible MEKDD$^{S217D/S221D}$ (MEK1) cell lines

Cell lines were transduced with lentiviral pInducer20/MEKDD construct and selected with Neomycin (G418) (200–800 μg/ml) every 2–3 days for 10–14 days. MEKDD$^{S217D/S221D}$ was induced by the addition of Doxycycline Hydrochloride (Cat# BP26531) (0.5 μg/ml) every 2 days and confirmed on protein level by blotting for phospho-ERK1/2 (T202/Y204).

Phosphokinase array

H720, H69 and H82 transduced with doxycycline-inducible MEKDD were cultured and harvested after 24 h upon MAPK activation. Relative levels of human protein kinase phosphorylation (43 human kinases) were detected using the Proteome Profiler Human Phospho-Kinase Array Kit (R&D, ARY003C) according to manufacturer's instructions. 400 μg protein were used per sample and image developed using the iBright Western Blot Imaging System (ThermoFisher). Pixel density was quantified using ImageStudioLite software.

Cell images

Pictures of suspension and adherent cells were taken with EVOS® FL Cell Imaging System (Thermo Fisher Scientific).

RNA extraction, sequencing, and analysis RNA_seq analysis

RNA extraction, sequencing and analysis were performed as in Wohlhieter et al. (2020). Briefly, QIAGEN RNeasy Plus Universal mini kit (QIAGEN, Hilden, Germany) was used to extract total RNA from cell pellets

according to manufacurer's instructions and RNA sequencing libraries prepared using NEBNext Ultra RNA Library Prep Kit for Illumina following manufacturer's instructions (NEB, Ipswich, MA, USA). RNA sequencing libraries were sequenced on the Illumina HiSeq instrument (4000 or equivalent; a 2x150bp Paired End (PE)) according to manufacturer's instructions.

Histology

Formalin-fixed paraffin embedded tissues were used to obtain 4μm sections for H&E staining. All slides were scanned in Aperio AT2 digital whole slide scanner and reviewed with Aperio ImageScope v12.4.3.7005 by an experienced pathologist.

CRISPR/Cas9

Small guide RNAs (gRNAs) targeting HES1, JAG1 and non-targeting control (NTC) were designed using the CRISPR design tool GuideScan (Perez et al., 2017) (www.guidescan.com) and chosen based on high targeting scores and lowest probability of off-target effects. gRNAs were validated by protein expression. gRNAs were cloned into lentiCRISPRv2 using Zhang lab protocol (genome-engineering.org, rev20140509). lentiCRISPR v2 was a gift from Feng Zhang (Addgene plasmid # 52961; http://n2t.net/addgene:52961; RRID:Addgene_52961) (Sanjana et al., 2014).

QUANTIFICATION AND STATITICAL ANALYSIS

GraphPad (GraphPad, Software, San Diego, CA, USA) was used to analyze data. Data represent the mean ± SEM as indicated in figure legends. In all experiments where two conditions are being compared (Figures 1B, 1E, 1F, 1H, 2E, 2F, 3A, 2B, 2D, 4C, 4F, S1E, S2B, and S2D) significance was established using unpaired t test where ns > 0.05, *p < 0.05, **p < 0.01, ***p < 0.001, ****p < 0.0001 or as otherwise indicated in the Figure.

For Figures 1A and S1A, p value was derived from Pearson's Chi-squared test and is shown in the Figure. For Figures 1G, 1I, and S1F, p value was calculated by log-rank test and is shown in the Figure.